Supporting Information

DNA-Mediated Self-Assembly of Plasmonic Antennas with a Single Quantum Dot in the Hot-Spot

Francesca Nicoli, Tao Zhang, Kristina Hübner, Boyuan Jin, Florian Selbach, Guillermo Acuna, Christos Argyropoulos, Tim Liedl, and Mauricio Pilo-Pais*

F. Nicoli, T. Zhang, T. Liedl, and M. Pilo-Pais
Faculty of Physics and Center for Nanoscience (CeNS), Ludwig-Maximilians-Universität München (LMU), Munich, Germany
E-mail: m.pilopais@lmu.de
T. Zhang Present address: Max-Planck-Institute for Intelligent Systems, Stuttgart, Germany

K. Hübner and F. Selbach,
Department of Chemistry and Center for Nanoscience (CeNS), Ludwig-Maximilians-Universität München (LMU), Munich, Germany

B. Jin and C. Argyropoulos
Department of Electrical and Computer Engineering, University of Nebraska-Lincoln, Lincoln, Nebraska, United States

G. Acuna
Department of Physics, University of Fribourg, Fribourg, Switzerland

Supporting Note 1. Antenna Assembly

DNA Sequences

DNA was purchased from Eurofins genomics LLC unless otherwise indicated. Strands used for NP functionalization can be divided into three segments: a functional group or sequence attached to the NP (red), a hybridization sequence (black), and a DNA spacer (green). Lower letters indicate phosphothiolated (PTO) bases and SH-C6 is a thiol- 6 carbon linker.

Nanoparticle	DNA sequence 5' to 3'
40 nm Au and 40 nm Ag	SH-C6 TT CTC TAC CAC CTA CAT
5 nm Au	ATG TAG GTG GTA GAG AA cgg gcg tgc
QD	ATG TAG GTG GTA GAG AA GGG GGG GGG

Table S1: DNA sequences used to functionalize AuNPs and QDs displaying the functional group or sequence attached to the NP (red), hybridization sequence (black), and DNA spacer (green).

Sample purification

The QD-antennas fabricated with conventional AuNPs or ultrasmooth spherical NPs were assembled by mixing QDs and AuNPs priorly functionalized with DNA at a 1:5 QD:AuNPs ratio in 1xTE with 5.5 mM Mg^{2+} buffer (40 mM Tris, 1 mM EDTA and 5.5 mM $MgCl_2$). Incubation was performed overnight, and the samples were then purified using gel electrophoresis.

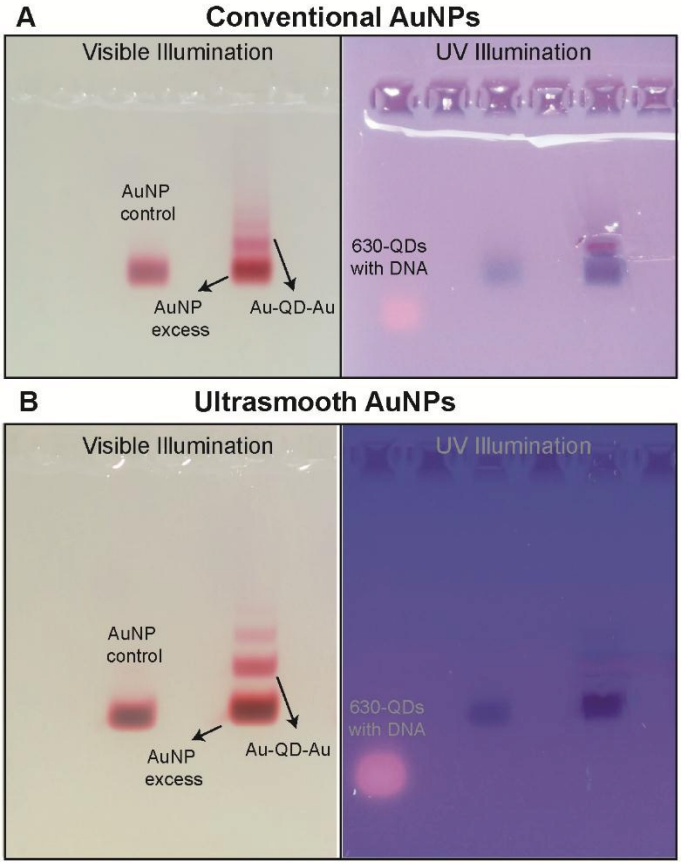

Figure S1: Gel purification and TEM imaging of the sample. Gel images of antennas made with **(a)** conventional AuNPs and **(b)** ultrasmooth AuNPs taken with visible light (left) and UV light (right). The gold dimer band is visible with regular ambient light due to the red color of AuNPs. The fluorescence from QDs band (control lane) is visible only under UV illumination.

TEM imaging of antennas

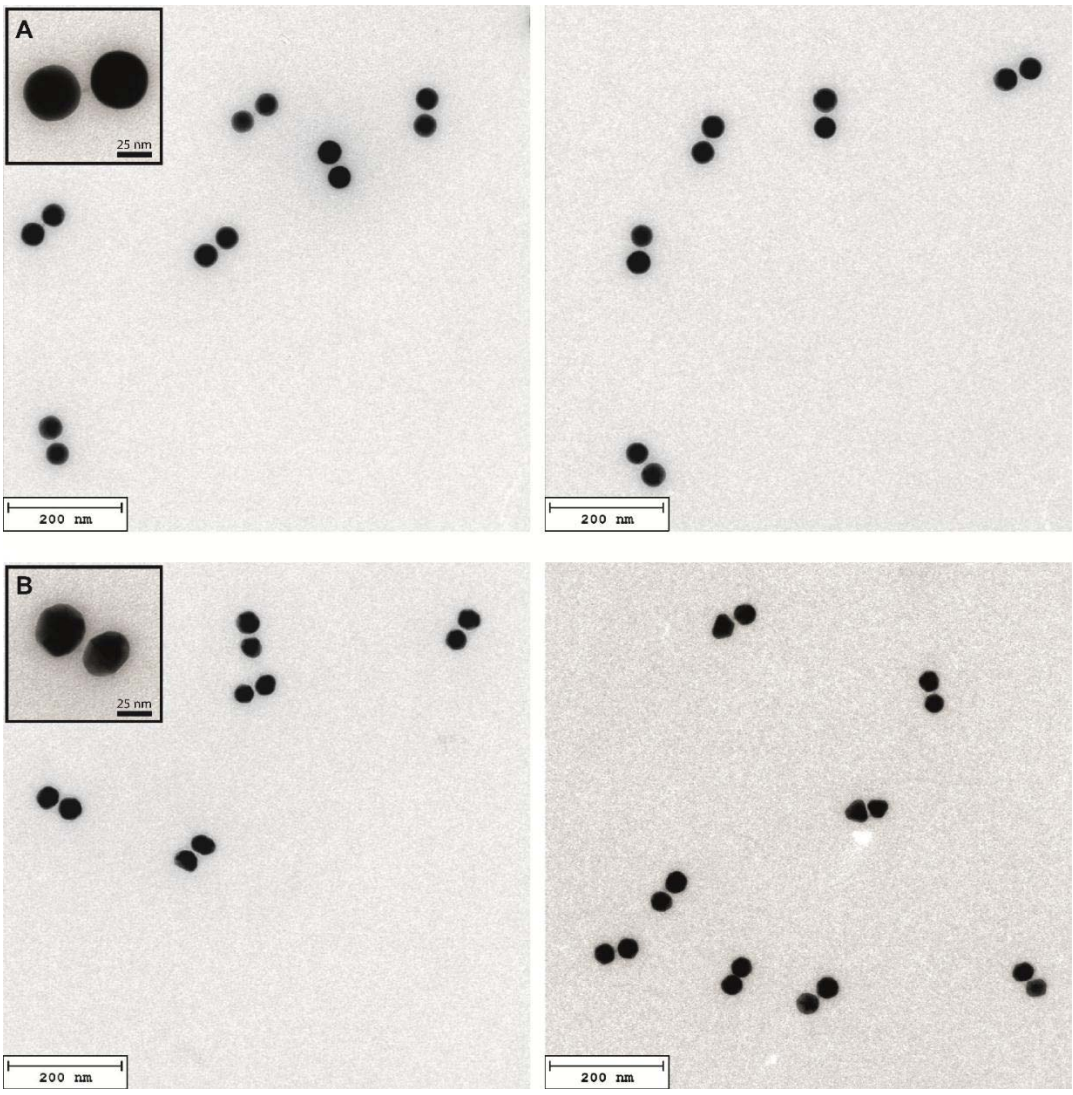

Figure S2: TEM imaging of 40 nm AuNPs antennas. Zoom-out TEM image of QD-antennas extracted from the gel with **(a)** ultrasmooth and **(b)** conventional NPs. Due to the high contrast of AuNPs it is challenging to see the QDs.

Supporting Note 2. Yield of Correctly Assembled Antennas

Number of QDs in the gap

To quantify the number of small NPs located in the gap of the antenna, we examined ~ 100 constructs using TEM. Although QD-antennas display a clear gap, indicating the presence of a QD between the NPs, the low contrast of the QDs when in presence of 40 nm AuNPs under TEM makes it challenging to accurately perform a count histogram of the number of QDs between the NPs. To get an impression of the gap size, we looked at N = 74 antennas and obtained a gap of ~4.5 nm ± 1.4, indicating the prescence of at least one QD in the gap (Figure 3). We then analyzed the analogue assembly of the antennas but with a 5 nm AuNP in the gap, which is clearly visible and further validates the generality of our assembly methodology. The histogram in Figure S4 shows that as one increases the $Large_{NP}$:$Small_{NP}$ ratio, the chances of having more than one $Small_{NP}$ in the gap decreases, as expected. For the optical measurements, we assembled all structures using a ratio of at least 5:1.

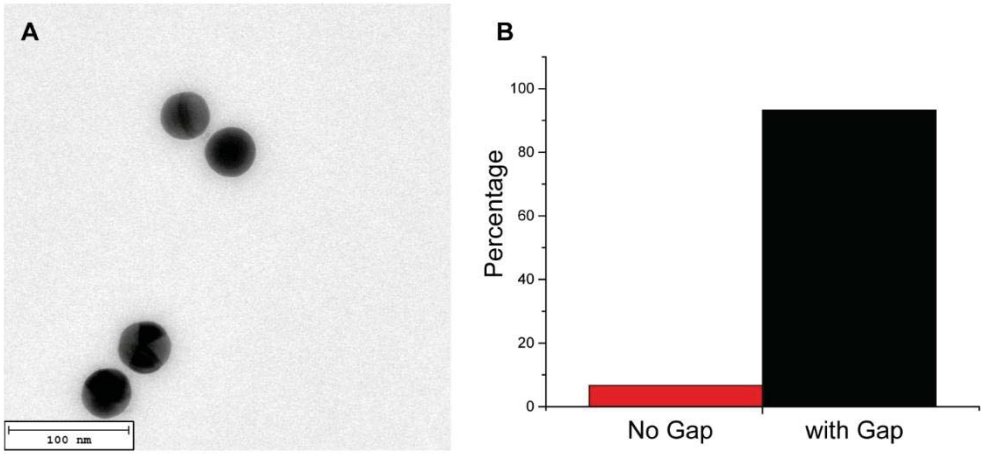

Figure S3: Number of Antennas displaying a gap. (a) TEM of antennas assembled using QDs. The QD is not always visible due to their low contrast in respect to AuNPs. **(b)** Histogram showing the number of dimers with and without measurable gap (N = 74).

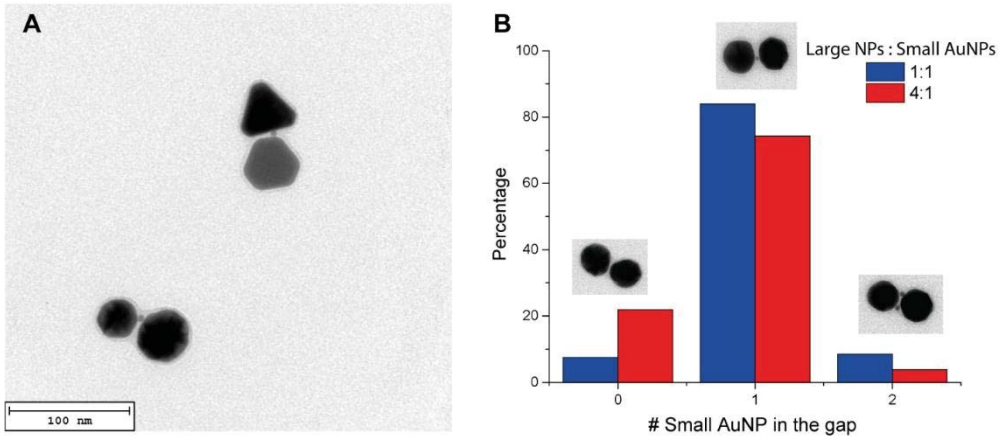

Figure S4: Number of Small AuNPs (5 nm) located in the antenna gap. (a) TEM of antennas assembled using 5nm AuNPs. The 5nm AuNP is always visible unless been "squeezed out" underneath the NPs (see Supporting Note 3). **(b)** For each $\boldsymbol{Large_{NP}}$: $\boldsymbol{Small_{NP}}$ ratio, $\sim\mathbf{100}$ dimers were classified according to the number of Small NPs (5 nm AuNP) in the structure. TEM insets are visual representations of the assembly type.

Higher order structures

Higher-order structures corresponding to the 3rd band (**of Au-[QD-Au]$_2$**) showed mostly linear conformations.

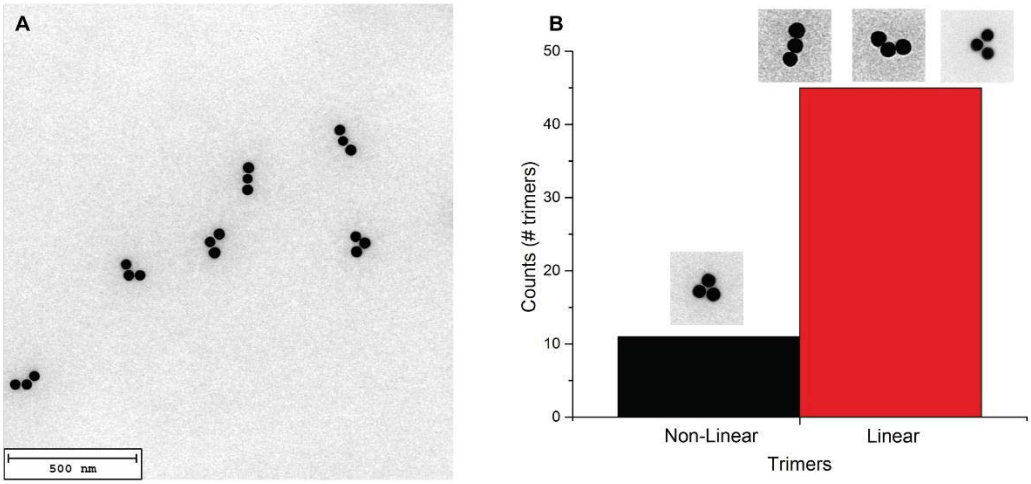

Figure S5: Yield analysis of Au-[QD-Au]$_2$ antennas. (a) Exemplary zoom-out TEM image of trimers after gel extraction (3rd band in Figure 1). **(b)** Yield of linear vs non-linear conformations. TEM insets are visual representations of the assembly type.

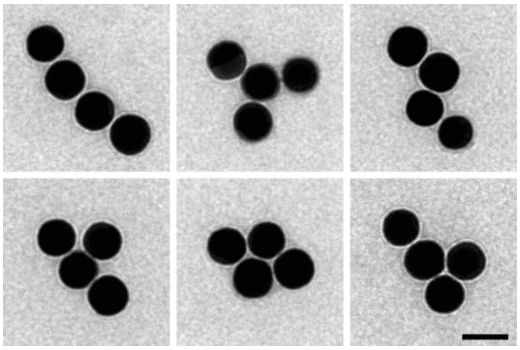

Figure S6: Yield analysis of Au-[QD-Au]$_3$ antennas. (a) Exemplary species of Au-[QD-Au]$_3$ after gel extraction (4th band in Figure 1). All species are found in equal yield. The gap is less clear due to a zoom-out artifact from the TEM. Scale bar 50 nm.

Assembly with Silver NPs

To test the flexibility of the assembly approach, we fabricated QD-antennas with silver (Ag) NPs and a 490 nm emission QD. Conventional AgNPs poses a more intrinsic shape variability than their AuNP counterparts.

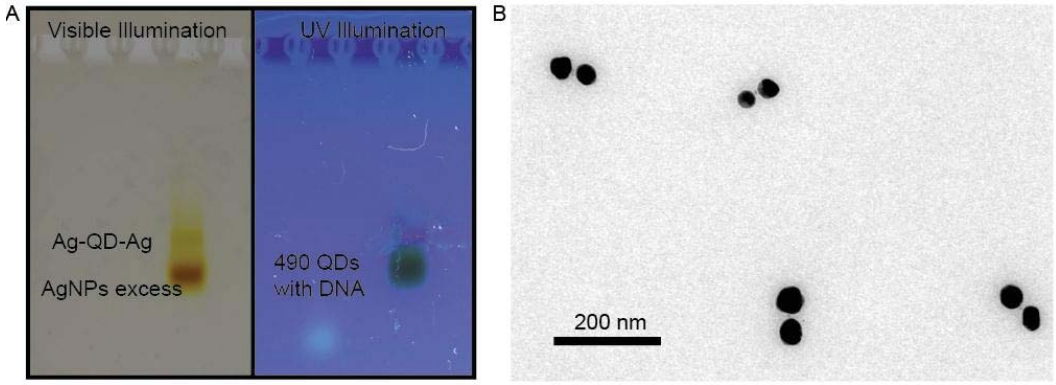

Figure S7: QD-silver antennas. Gel purification and TEM imaging of silver antennas. **(a)** Images of the gel taken with visible light (left) and UV light (right). **(b)** TEM image of QD-Ag Antennas. Since silver has a lower contrast under TEM than AuNPs, it is easier to observe the QDs between the AgNPs in comparison to AuNPs.

Supporting Note 2. Proof of Assembly Principle Using Steric-Hindrance

To test the steric hindrance principle limits on which the antenna assembly is based, we built structures with smaller AuNPs (10 nm and 15 nm). As the radius of the NPs gets closer to the one of the QD (~5 nm), non-linear conformations become predominant such as conformations displaying angles (α) smaller than 180 degrees (Figure S8a) or structures where steric-hindrance no longer prevents more than two $Large_{NPs}$

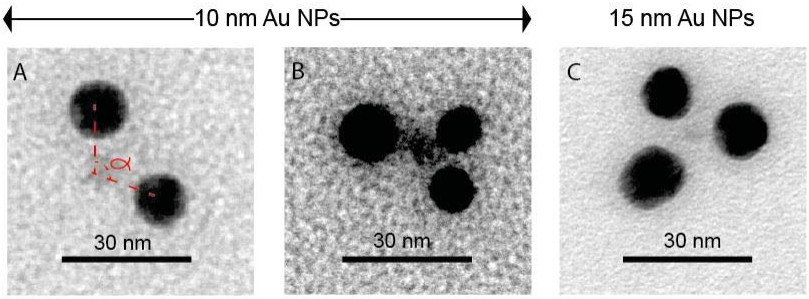

attaching to the $Small_{NP}$ (Figure S8b and S8c).

Figure S8: TEM imaging of AuNPs-QD constructs with 10 and 15 nm AuNPs displaying non-linear conformations. **(a)** Exemplary Au-QD-Au structure displaying a large opening angle ($\alpha < 180°$), and **(b)** 10 nm and **(c)** 15 nm AuNPs constructs where steric-hindrance no longer applies. QD is $\sim 5\ nm$.

Supporting Note 3. Conformational Changes of the Antenna Structures on Surfaces

Dark-field (DF) spectroscopy measurements show a plasmon resonance lying in a range from 2.05 to 2.25 eV. We attribute these spread mainly to conformational variations from antenna to antenna acquired when deposited on the substrate surface, and AuNP quality (e.g. facets, size variation). TEM imaging corroborates the gap variability when using conventional NPs (Figure S9 upper panel) which in turn shifts the location of the QD inside the gap. Since our samples are dried after substrate deposition, initial landing and subsequent drying of the antennas on the TEM grid or substrate interactions affect the ultimate dried conformation. Surprisingly, this effect is rarely observed when using ultrasmooth NPs, which suggests that capillary forces are exacerbated by the presence of facets. During surface deposition, a droplet of sample is incubated for a few minutes, followed by droplet removal using an absorbing paper, and subsequent drying at room temperature (TEM grid deposition) or blow dried by a stream of nitrogen gas (glass slide deposition). During the drying process, remaining liquid in the vicinity of the structures slowly evaporates, which leads to shrinking of the liquid meniscus around the particles and capillary forces acting on the particles.[1,2]

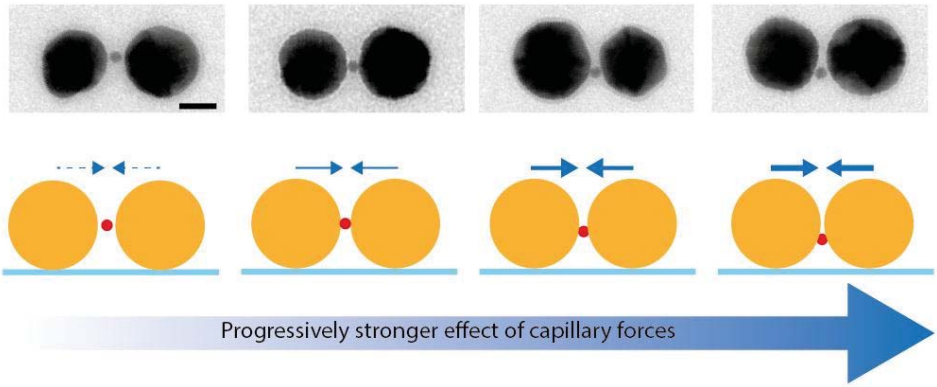

Figure S9: Antenna conformations. Exemplary TEM images and schemes of different conformations of the QD-antennas when using conventional NPs, after deposited on a surface and dried. We attribute this effect to capillary forces exacerbated by the presence of facets existing in conventional NPs. Constructs formed using ultrasmooth NPs on the other hand, display a more robust configuration, with the QD sitting preferentially in the middle. The small blue arrows indicate the progressively stronger effect of capillary forces due to drying (depicted with the big blue arrow).

Supporting Note 4. QDs Bulk Spectral Properties

We measured the bulk absorption and emission spectra of the QDs functionalized with the respective DNA sequence (see Table S1). The absorption measurements were performed using a 10 mm optical path length quartz cuvette (Hellma-analytics) and a V-650 Spectrometer (Jasco) with 1 nm resolution and 1 s/point integration time. Bulk fluorescence measurements were carried out with a cuvette 2 × 10 mm optical path (Hellma-analytics) using a modular spectro-fluorometer Fluorolog3 (Horiba Scientific).

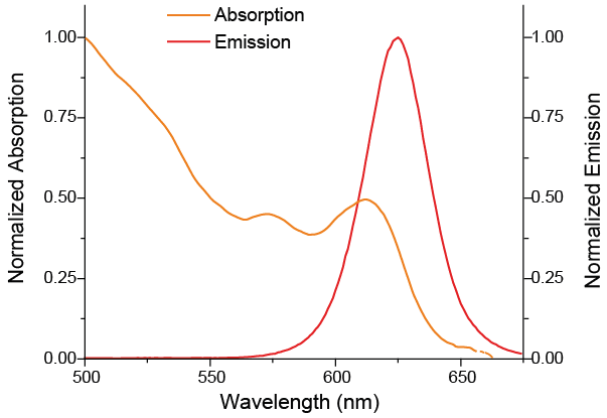

Figure S10: QDs optical properties. Bulk absorption (orange) and emission (red) spectra of DNA-functionalized 630-QDs.

Supporting Note 5. Fluorescence Traces Analysis

The analysis of fluorescent traces was performed using a Matlab script. In brief, each measurement contains 4000 frames (400 s, 0.1 s acquisition rate). All the frames were averaged and used to manually localize the fluorescent spots. For each spot, an area of 5x5 pixels was considered and the background averaged over four adjacent areas (5x5 pixels) was subtracted. Time traces plots were obtained by performing this procedure over each of the 4000 frames. A baseline signal attributed to scattering of the AuNPs was later subtracted. A similar baseline is observed in the control experiments (Supporting Note 8).

Supporting Note 6. Epi-fluorescence – Dark-field – SEM correlation

The correspondence between fluorescence time traces, plasmon resonances, and SEM imaging was performed as follows:

1. Before fluorescence measurements, we located the area of interest within the sample delimited by markers on the glass slide (scratches made with a scriber before glass slide cleaning). This area was located looking at the CCD using light ambient conditions (laser off).
2. We then proceeded to record fluorescence emission (laser on).
3. The sample was then transferred to a dark-field microscope where we acquired the scattering images and spectra of the same areas measured with epi-fluorescence.
4. We established a correspondence between scattering signal and fluorescence emission spots (see Figure 4a).
5. SEM mapping of the areas of interest was performed and each antenna was located. The structures were identified from spatial triangulation from the markers on the glass slide.

Supporting Note 7. Theoretical Calculation

Full-wave three-dimensional simulations of the QD-antennas were performed using the commercial finite-element simulation software COMSOL Multiphysics. The scattering was simulated from the scattered-field formulation, in which we obtained the scattered fields by subtracting them from the analytical solution of an incident plane wave in the absence of the dimer (background field). The field enhancement, shown in Figure S11D, was computed at the resonance frequency of the QD-antenna scattering response. The incident excitation wave is always perpendicular to the plane formed by the QD-antenna. The permittivity of gold varies with frequency and is extracted from experiment data.[5] The glass substrate has a refractive index n = 1.45. In general, the fluorescence enhancement factor can be described as the multiplication of several factors computed by theory and experiment and its value is given by the formula:[6]

$EF(\vec{r}) = \frac{\eta}{\eta_o}\frac{\gamma_{ex}(\vec{r},\theta)}{\gamma_{ex}^{o}(\vec{r},\theta)}\frac{QY(\vec{r})}{QY_o}$ where η is the emission collection efficiency, γ_{ex} is the excitation rate computed at the excitation frequency of the system (2.21 eV), QY is the quantum yield, $\vec{r}$ is the space vector, $QY_0 \sim 5\%$ is the intrinsic quantum yield of the used QDs, and θ is the polar orientation of the emitter's dipole. In the current work, our goal is to compute the trend of fluorescence enhancement to provide some further physical insights to better explain the experimental results presented in the main text. Hence, we use a simplified version of the previously presented fluorescence enhancement formula $\langle EF \rangle \approx \langle \gamma_{ex}/\gamma_{ex}^{o} \rangle \langle QY/QY_o \rangle$ to compute the trend of the fluorescence enhancement. The quantum yield is defined as:

$QY = k_{rad}/(k_{rad} + k_{nrad})$, where k_{rad} and k_{nrad} are the radiative and non-radiative recombination decay rates, respectively. The average $\langle QY \rangle$ can be computed by full-wave simulations where the QD emitter is modelled as a point-dipole with a fixed orientation along the dimer gap.[7] In our simulations, we calculated the Green function originating from the dipole which is assumed to emit monochromatically at the resonance of the gold dimer. The radiative rate can be derived by integrating the power outflow through the boundaries of the simulation domain. The non-radiative rate, on the other hand, is the volume integral of the absorbed power along all the lossy materials. The computed QY for dimers with different gaps is plotted in Figure S11A. The average excitation rate enhancement $\langle \gamma_{ex}/\gamma_{ex}^{o} \rangle$ is given by the ratio of the

maximum field enhancement when the dimer antenna is present over the field enhancement without the antenna computed at the excitation frequency of the system (2.21 eV). The maximum field enhancement is plotted in Figure S11B and is found to be maximum for the 6 nm QD-antenna gap case. When the QY and maximum field enhancement, presented in Figures S11A and S11B, respectively, are multiplied by using the previously mentioned simplified version of the fluorescence enhancement formula, the trend of the average fluorescence enhancement is obtained, as shown in arbitrary units in Figure S11C. We clearly demonstrate by full-wave simulations that the maximum fluorescence is expected for a QD-antenna gap thickness equal to 6 nm, similar to the presented experimental results. Au dimers assembled with the QD and with the DNA origami display the same plasmon resonance scattering ($\sim$585 nm). Addition of the QDs permittivity in the simulations resulted on a negligible shift on the scattering peak position.

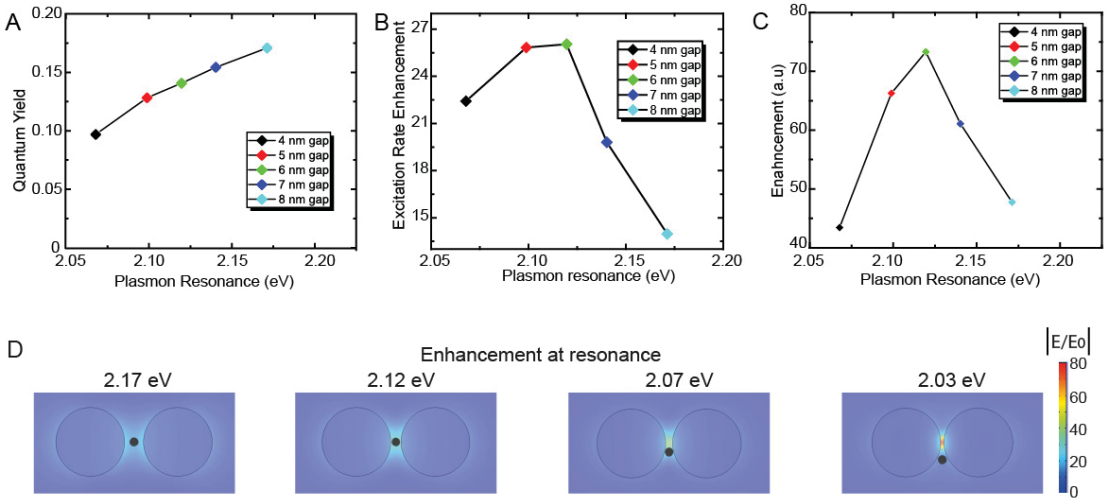

Figure S11: Simulation results of the QD-antenna system for different gaps. The computed **(a)** quantum yield (QY), **(b)** average excitation rate (maximum field enhancement) at the excitation frequency, and **(c)** the normalized fluorescence enhancement trend are given in arbitrary units. **(d)** Calculated electric field enhancement at different plasmon resonances corresponding to nominal gap sizes of 8, 6, 4, and 2 nm (from left to right). The energy of the incident field is 2.21 eV (561 nm), equal to the laser line used in the epifluorescence experiments.

Supporting Note 8. Control Experiment: AuNPs Dimer Mediated by DNA Origami

The assembly of the AuNPs dimer control is mediated by a 2-layer sheets DNA origami structure with capture DNA strands on both sides of the block, so that one NP functionalized with the complementary sequence docks on each side. The DNA origami which is sandwiched between the particles serves as a gap spacer, as described in detail in Roller *et al.*[8] We estimate the gap size to be ~ 5 nm, similar to the QD diameter and gap size of the QD-antenna structures. The sample was gel purified, the assembly verified by TEM imaging (Figure S12), and subsequently deposited on a glass slide. The fluorescence and DF measurements were carried out as for the QD-antennas. No emission from gold or potential buffer contaminants was observed other than a constant baseline which we attribute to scattering (Figure S13). This scattering is also observed on the QD-antenna and it is subtracted from the emission traces.

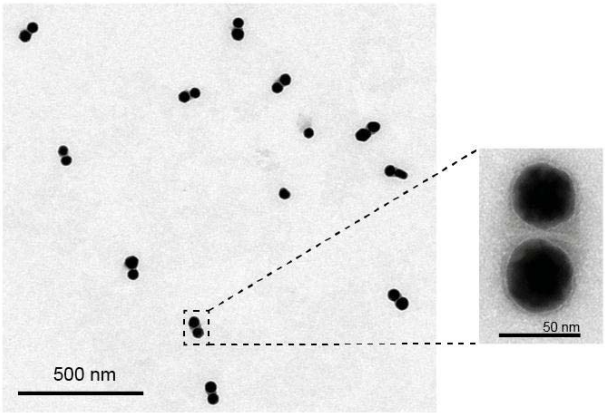

Figure S12: Control sample. TEM imaging of the control structure, consisting of a 40 nm AuNPs dimer assembly bridged by a 2-layer DNA origami block. The spacing between the NPs is of ~5 nm.

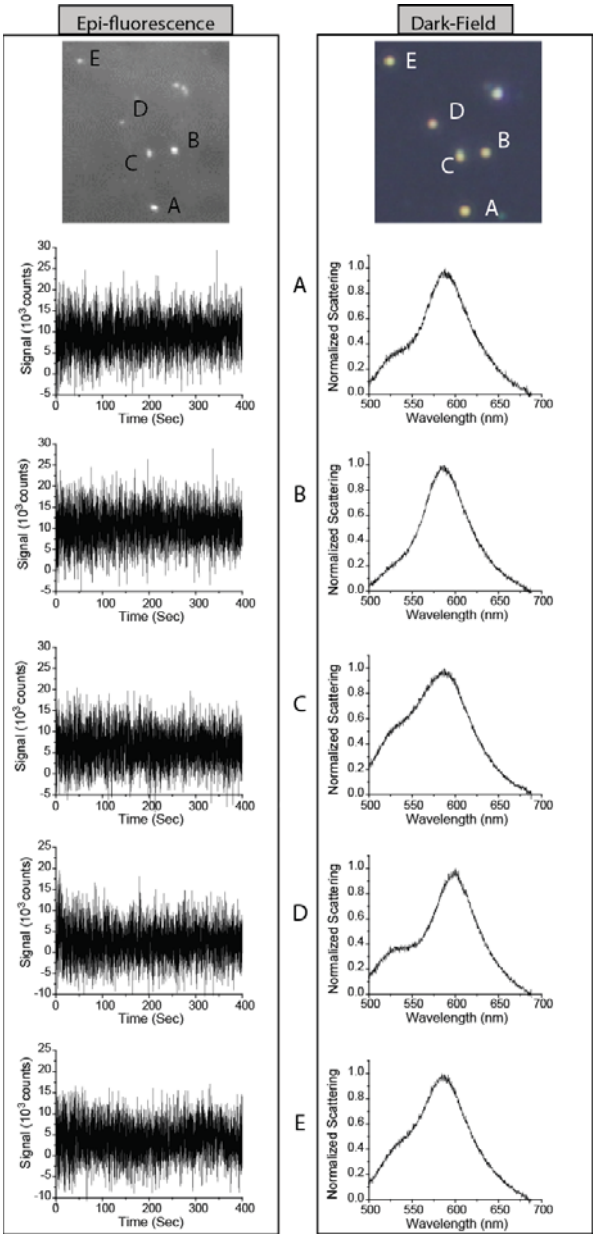

Figure S13: Epi-fluorescence and DF measurements of representative AuNP-origami control structures. Wide-field image accompanied by the corresponding time trace and the scattering spectrum of each individual structure.

Supporting Note 9. Additional Data

Quantum dots emission

The data shown in Figure S14 corresponds to the epi-fluorescence emission of QDs functionalized with DNA (sequence reported in table S1). Characterizing individual QDs on a surface is challenging due to the presence of potential contaminants[3] and the collective emission[4] effects of nearby QDs. In addition, the QDs used on this study have a QY of 5% which makes them challenging to be observed at low excitation powers. To achieve single QD characterization, we prepared a series of glass slides with progressively higher dilutions (one order of magnitude per dilution) and observed the changes in the density of fluorescence spots. We analyzed the sample which was diluted enough to show well-spaced fluorescence spots. Despite these efforts, few traces displayed no off-behavior, which could be due to more than one QD been present in the analyzed region. As a further control, we used an empty glass slide without QDs but exposed to the same conditions (e.g. plasma etching, buffer, washing) and found no detectable fluorescence. All the glass slides were cleaned by sonication in acetone followed by sonication in isopropanol. Right before sample deposition, the surface was further cleaned and charge-activated by oxygen plasma. The mean fluorescence emission of the QDs is an overestimate, since several less bright QDs could be below our detection limits.

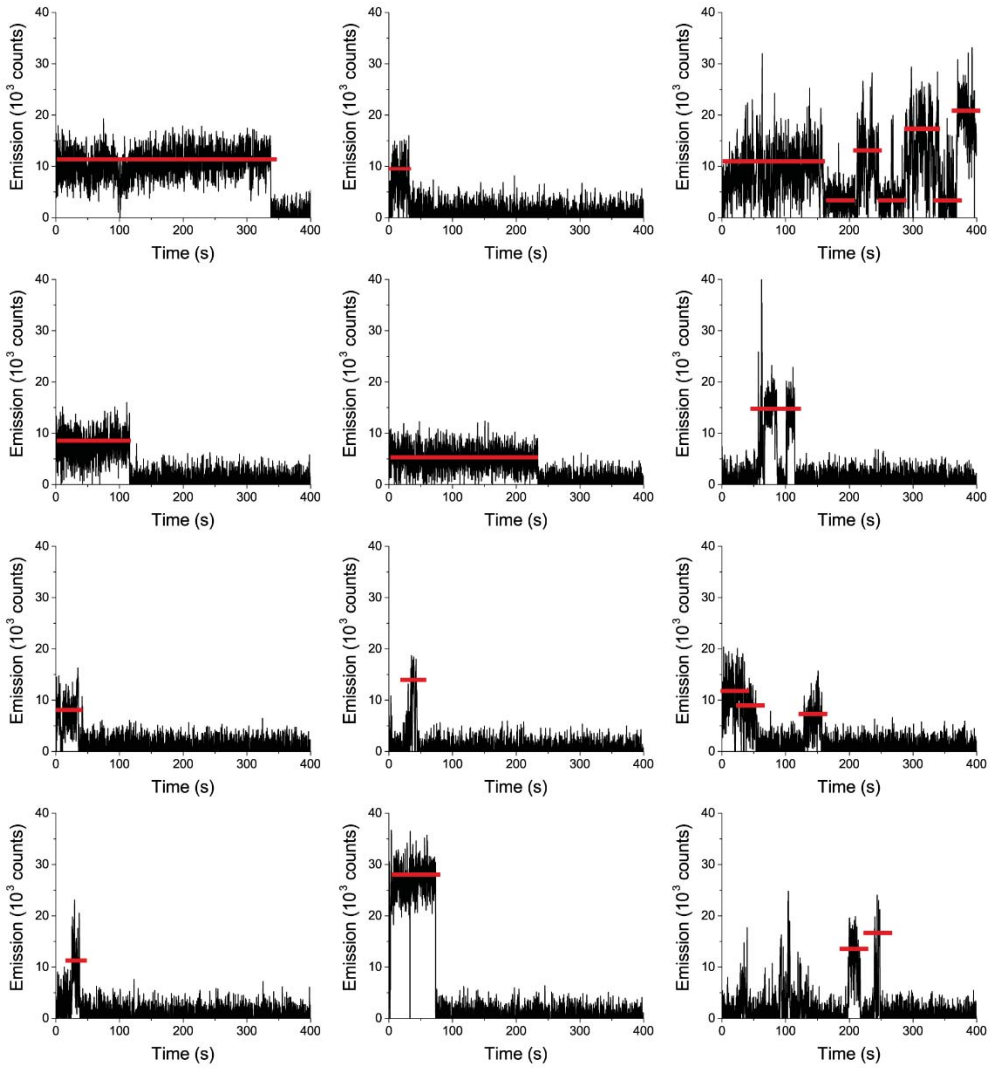

Figure S14: Measurement of QDs. Epi-fluorescence traces of DNA functionalized QDs. The mean emission is of $12.3\ x10^3$ counts.

Fluorescence and scattering traces of all structures measured

All data shown in Figure 6 is correlated by superimposing fluorescence and dark-field images, as described in the main manuscript and Supporting Note 15-16. Each individual structure made with conventional AuNPs is additionally correlated with SEM imaging to ensure that all reported structures are dimers. In some limited occasions, SEM revealed that the structure of interest corresponded to individual triangles, trimers, or two closely spaced dimers. On the other hand, antennas fabricated using ultrasmooth spherical AuNPs displayed a consistent plasmon resonance which together with polarization measurements is enough to ensure that the structure corresponds to a well-formed individual dimer.

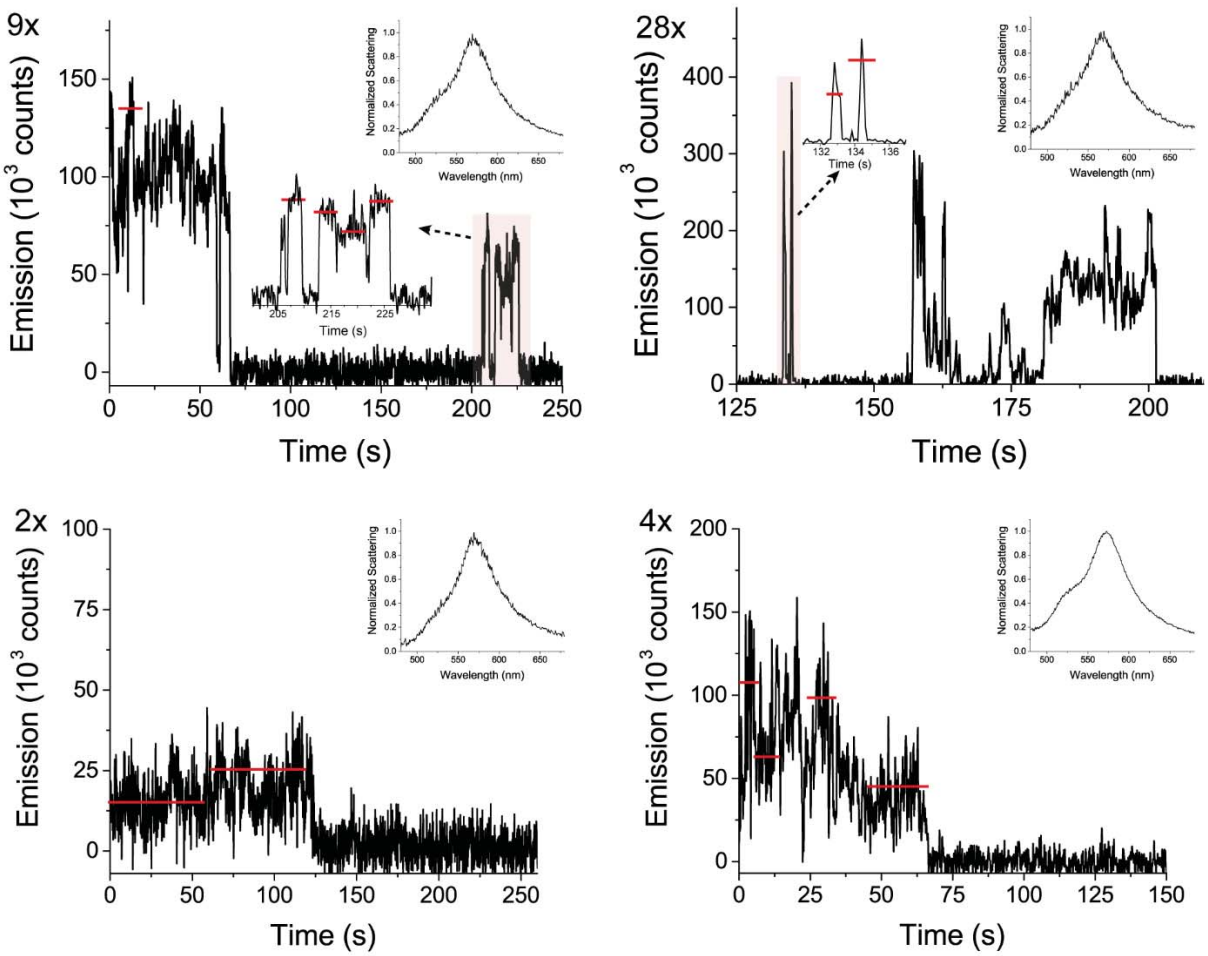

Figure S15: Measurement of antennas fabricated with ultrasmooth spherical NPs. Epi-fluorescence traces of each ultrasmooth spherical AuNPs antenna measured, with the respective plasmon scattering signal. The blue shadow and red bar indicates the area and value used to calculate the enhancement in respect to individual QDs.

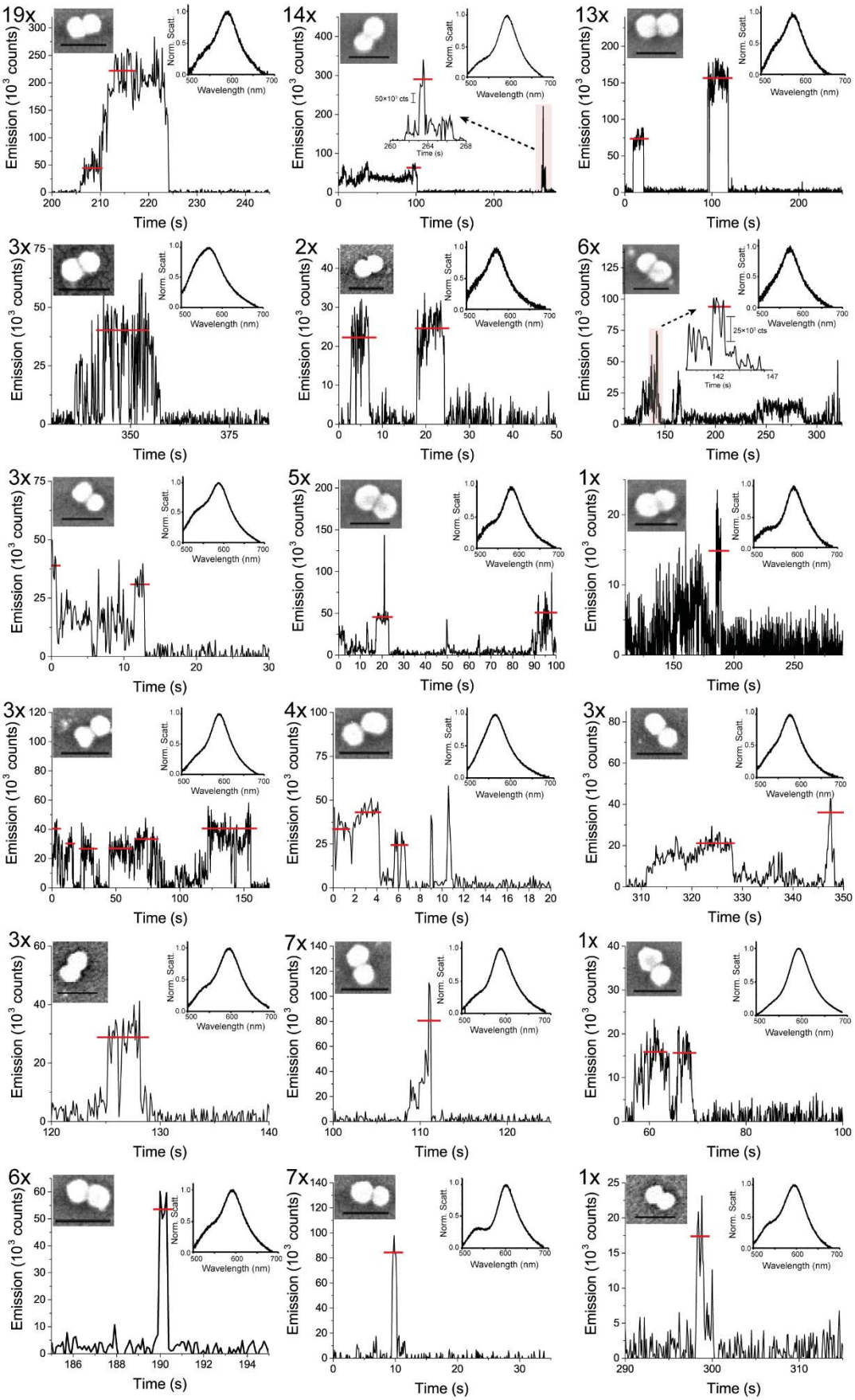

Figure S16: Measurements of all antennas fabricated with conventional AuNPs. Epi-fluorescence traces of each structure measured, with its respective plasmon scattering and SEM image (scale bar 100 nm).

Supporting Note 10: Lifetime Measurements

Lifetime measurements were performed using a confocal microscope as described in Materials and Methods. For sample deposition, the cover-slides were incubated with a 1 mg/mL BSA-Biotin solution for 15 min. Subsequently, a 1 mg/mL neutravidin solution was then added for 10 min. Finally, a 100 nM solution of the single stranded DNA sequence, complimentary to the sequence used for functionalizing the NPs and labelled with biotin was deposited for 10 min. Rinsing three times with 0.5 X TE buffer and 5.5 nM $MgCl_2$ was performed between all incubation steps. Samples were then incubated and the density was monitored on the confocal microscope. Afterwards, remaining samples in solution were washed with buffer and dried under a nitrogen flow.

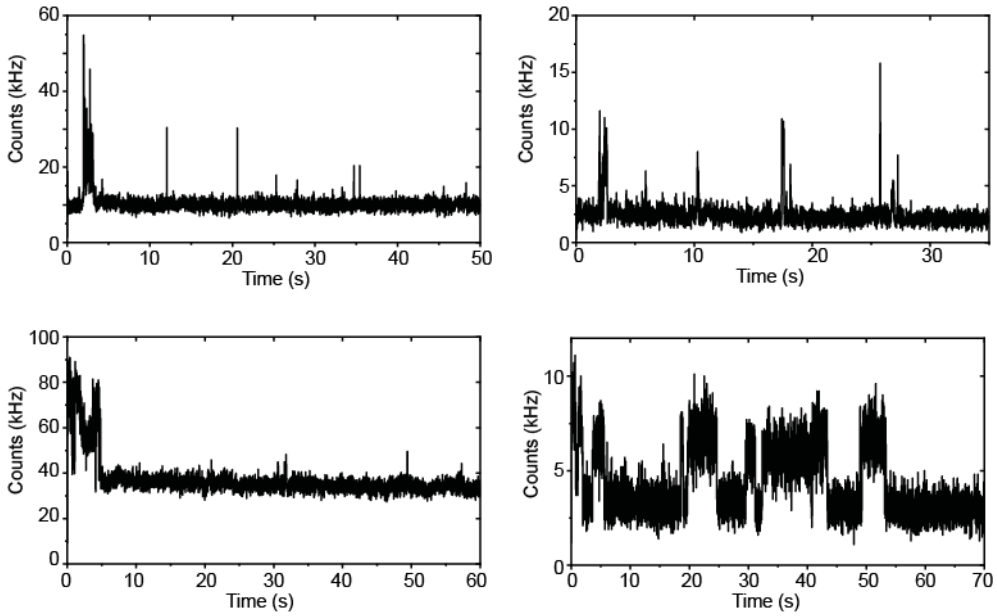

Figure S17: Emission traces of antennas. Confocal fluorescence traces showing the scattering of the gold nanoparticles and additional blinking of the quantum dots.

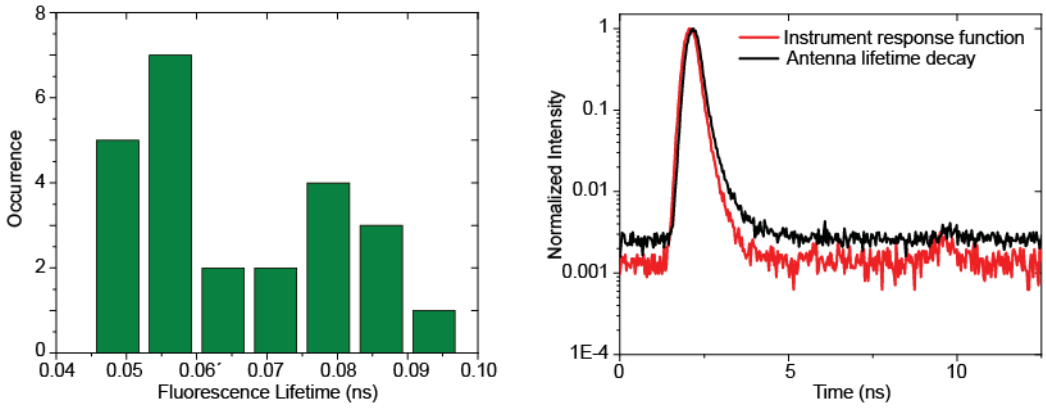

Figure S18: Fluorescence lifetime of antennas. Histogram of deconvoluted fluorescence lifetimes (left) with a mean value of 0.065 ns. Right graph shows a fluorescence lifetime decay (black) compared to the instrument response function (red).

References

[1] B. Nikoobakht, Z. L. Wang, M. A. El-Sayed, *J. Phys. Chem. B* **2000**, *104*, 8635.

[2] Z.-C. Xu, C.-M. Shen, C.-W. Xiao, T.-Z. Yang, S.-T. Chen, H.-L. Li, H.-J. Gao, *Chem. Phys. Lett.* **2006**, *432*, 222.

[3] X. Wang, X. Ren, K. Kahen, M. A. Hahn, M. Rajeswaran, S. Maccagnano-Zacher, J. Silcox, G. E. Cragg, A. L. Efros, T. D. Krauss, *Nature* **2015**, *527*, 544.

[4] M. Scheibner, T. Schmidt, L. Worschech, A. Forchel, G. Bacher, T. Passow, D. Hommel, **2007**, DOI 10.1038/nphys494.

[5] G. Ghosh, E. D. Palik, *Handbook of Optical Constants of Solids*, Academic Press, **1985**.

[6] T. B. Hoang, G. M. Akselrod, C. Argyropoulos, J. Huang, D. R. Smith, M. H. Mikkelsen, *Nat. Commun.* **2015**, *6*, 1.

[7] C. Ciracì, A. Rose, C. Argyropoulos, D. R. Smith, *J. Opt. Soc. Am. B* **2014**, *31*, 2601.

[8] E.-M. Roller, C. Argyropoulos, A. Högele, T. Liedl, M. Pilo-Pais, *Nano Lett.* **2016**, *16*, 5962.